Chemical Science

ROYAL SOCIETY OF CHEMISTRY

EDGE ARTICLE

View Article Online
View Journal

Cite this: DOI: 10.1039/d6sc02973f

All publication charges for this article have been paid for by the Royal Society of Chemistry

Fluoride-substituted $Li_{6.4}La_3Zr_{1.4}Ta_{0.6}O_{12}$ with delocalized electron-share accelerates Li^+ desolvation kinetics for high-voltage lithium metal batteries

Peng Chen,[a] Bing Ding,[abc] Hui Dou *[abc] and Xiaogang Zhang [abc]

Metallic lithium is regarded as the ideal anode material for high-specific-energy batteries. However, the $Li(solvents)_x^+$ formation in the liquid-state lithium metal batteries (LMBs) results in sluggish ion transport kinetics and continuous interface deterioration. Herein, an ion-kinetics promoter with delocalized-electron-sharing is designed to reduce the desolvation energy barrier, accelerate interfacial lithium diffusion, and achieve a stable interface. Specifically, the F-substituting $Li_{6.4}La_3Zr_{1.4}Ta_{0.6}O_{12}$ (named as $LLZTO_xF_y$) breaks the electron-confined state of the original metal–O (M–O). It induces electron redistribution at the central metal sites, thereby releasing more delocalized electrons. The relationships between charge transfer and ionic desolvation under the delocalized-electron-shared type promoter are comprehensively understood through theoretical calculations and *in situ* characterization. The F-substitution activates the O–M–F site activity of $LLZTO_xF_y$, thereby enhancing the binding of solvent C=O bonds to these sites, resulting in a high Li^+ transference number (0.68). Consequently, the lithium–lithium symmetric cell based on $LLZTO_{0.95}F_{0.05}$@PP can stabilize cycling for 1400 h with a lower overpotential (7.3 mV). Meanwhile, the Li|$LLZTO_{0.95}F_{0.05}$@PP|$LiCoO_2$ full cell can retain a high specific capacity of 88.2% after the 500th cycle at 1.0C under a high voltage of 4.6 V. Therefore, this strategy contributes to achieving long-cycle stability of anodes in LMBs.

Received 10th April 2026
Accepted 17th May 2026

DOI: 10.1039/d6sc02973f

rsc.li/chemical-science

Introduction

Lithium (Li) metal has been considered a promising anode material for high-energy-density rechargeable batteries due to its high specific capacity (3860 mAh g^{-1}) and the lowest electrochemical potential (−3.04 V *vs.* standard hydrogen electrode).[1,2] However, uncontrolled Li dendritic formation and continuous interfacial side reactions lead to short lifespan, and safety hazards as well, especially under high working voltage and high current density.[3] The formation of $Li(solvents)_x^+$ through interactions between Li^+ and various solvents is considered the principal hurdle to internal/interfacial Li^+ diffusion in liquid-state Li metal batteries (LMBs), ultimately leading to unbalanced interfacial electrochemistry and local Li^0 accumulation (Fig. 1a).[4,5] Worse, the accumulated Li^0 will become incorporated by the metal lattice, forming the notorious Li dendrites.[6] That means reconstructing the structure of $Li(solvents)_x^+$ can help reduce the desolvation energy barrier and accelerate rapid interfacial Li^+ transmission.[7,8] Despite electrolyte engineering of tuning the local solvation shell, the desolvation energy barrier can be reduced by introducing an ion-kinetics regulator, and a fast Li^+ transport channel can be constructed between the $Li(solvents)_x^+$ and the Li anode, thereby promoting the Li^+ flux.[9,10]

Generally, the interfacial desolvation efficiency is related to the charge distribution and transfer rate on the surface of the ion-kinetics regulators. Conventional ion-kinetics regulators with a stable crystal structure induce electron confinement, decreasing local charge separation and transport rates and reducing the local activity (Fig. 1b).[11] As revealed in our previous work, replacing the O atom with an isoelectronic S atom can disrupt the original stable crystal structure and redistribute local charge, providing more short-range, faster charge-transfer channels.[12] However, precisely regulating charge distribution and developing advanced crystal structure design remain challenging. The theoretical proposal lacks further verification of the structure–activity relationships between microstructure and reaction kinetics.[13] Therefore, it is of great significance to know how to induce the delocalized charge redistribution by

[a]*Jiangsu Key Laboratory of Electrochemical Energy Storage Technologies, College of Materials Science and Technology, Nanjing University of Aeronautics and Astronautics, Nanjing 210016, P. R. China. E-mail: dh_msc@nuaa.edu.cn; azhangxg@nuaa.edu.cn*

[b]*Shenzhen Research Institute, Nanjing University of Aeronautics and Astronautics, Shenzhen 518000, China*

[c]*National Key Laboratory of Mechanics and Control for Aerospace Structures, Institute for Frontier Science, Nanjing University of Aeronautics and Astronautics, Nanjing 210016, P.R. China*

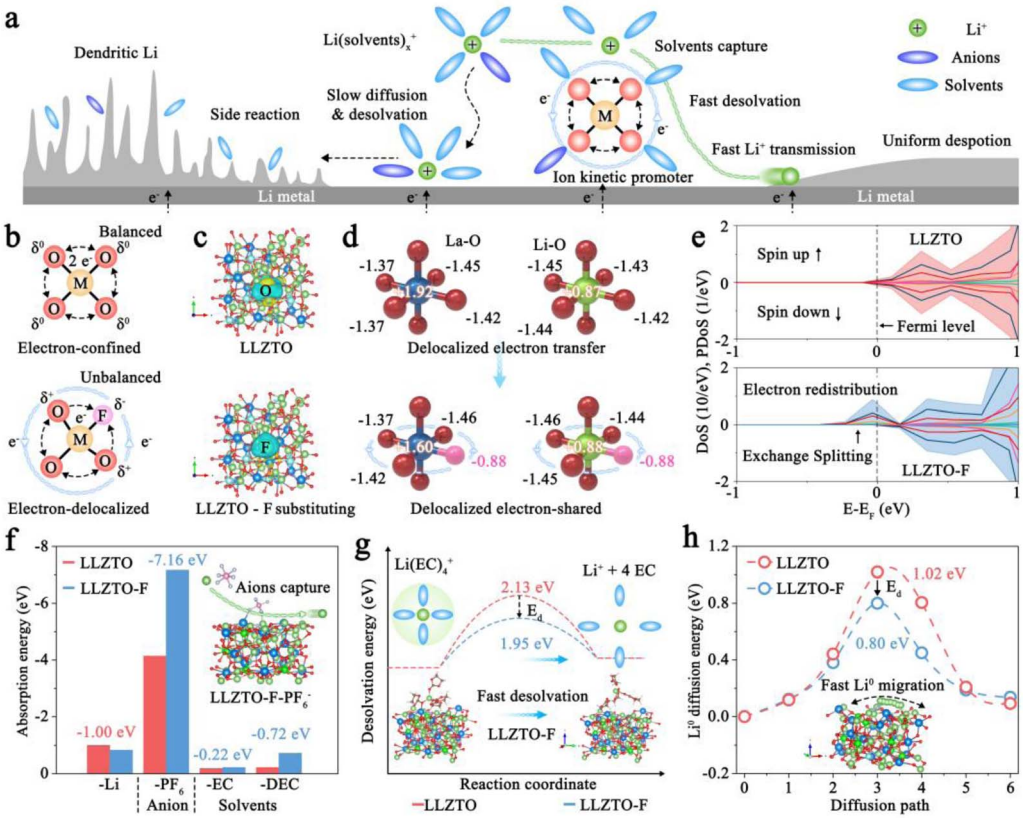

Fig. 1 (a) The interfacial desolvation evolution of Li(solvent)$_x^+$ species and Li$^+$ deposition with/without ion kinetic promoter. (b) Schematic diagram of electron-confined and electron-delocalized ion kinetic promoter. (c) Charge density difference of LLZTO and LLZTO-F. (d) Valence electron number of La–O and Li–O with/without F-substituting. (e) Partial density of states. (f) Absorption energy of Li, PF_6, and solvents on LLZTO and LLZTO-F. (g) Desolvation energy barrier and (h) Li^0 diffusion energy barrier on LLZTO and LLZTO-F.

regulating atomic substitution and the reconstruction of more efficient and shorter-range active sites in the microstructure.

Herein, we designed a delocalized-electron-shared (DES) ion kinetic promoter to accelerate desolvation kinetics by replacing the O atom with an F atom. With lower valent electron count (-2 e$^-$ *vs.* -1 e$^-$) and higher electronegativity (3.5 *vs.* 4.0), the unsaturated central metal sites exhibit a delocalized electron-sharing characteristic (Fig. 1b).[12] As a demo, the construction of the F-substituted LLZTO$_x$F$_y$ DES ion kinetic promoter by fluorination is designed on the fast Li$^+$ conductor $Li_{6.4}La_3Zr_{1.4}Ta_{0.6}O_{12}$ (LLZTO), serving as the polypropylene (PP) separator modification layer to effectively regulate the interfacial Li(solvents)$_x^+$ desolvation, Li$^+$ diffusion, and nucleation behaviors (Fig. S1). Consistent with theoretical calculations and *in situ* Fourier transform infrared spectroscopy (FTIR) results, the reconstruction of delocalized electron-active sites contributes to the breaking of the electron-confined state of the original O–metal–O (O–M–O), forming a stronger local electric field (O–M–F) that anchors the anions and solvents, thereby enhancing the stability of the Li anode. Thus, the Li||Li symmetric cell with $LLZTO_{0.95}F_{0.05}$@PP cycles stably for over 900 h without short-circuiting at 0.5 mA cm^{-2} and 0.5 mAh cm^{-2}. Notably, even when coupled with high-voltage $LiCoO_2$ (LCO, 3.0–4.6 V, 1.0C = 220 mAh g^{-1}) cathodes, the Li|$LLZTO_{0.95}F_{0.05}$@PP|LCO full cell retains a specific capacity of 100 mAh g^{-1} after 250 cycles at 4.0C. Moreover, the Li|$LLZTO_{0.95}F_{0.05}$@PP|LCO cell maintains a capacity retention rate of 94.5% after 120 cycles at 0.5C under 0 °C. Therefore, LMBs fabricated with the LLZTO$_x$F$_y$ DES ion kinetic promoter exhibited superior cycle life.

Results and discussion

Regulation of the electronic structure and transport pathways in the promoter is important for electrochemical performance.[14] With the local delocalized electron-shared states, more free electrons can participate in reactions, thereby increasing desolvation efficiency.[15] Based on these principles, we established models of LLZTO with F atom-substitution. We used density functional theory (DFT) calculations to investigate the effect of the kinetic promoter on electron delocalization, thereby enabling rapid Li diffusion. The charge-density difference in Fig. 1c indicates that the metastable M-O_3-F structure exhibits more efficient interfacial separation and transfer than the balanced M-O_4 structure in LLZTO, thereby forming atomic-level electron transport channels.[12] Moreover, substitution of F (with a valence electron of -0.88 eV) for O (-1.42 eV) alters the valence charge distribution around the central metal atoms, promoting more free electrons, thereby facilitating electron

delocalization (Fig. 1d). The projected density of states in Fig. 1e and S2 reveal that LLZTO-F exhibits a non-zero density of states at the Fermi level. The electrons occupy spin-up states, indicating that F-atom substitution enhances local electron transport in LLZTO. The models for Li^+, anions, and solvents on the LLZTO-F and LLZTO had been established, and the relevant adsorption energy, desolvation energy barrier, and surface diffusion energy barrier had also been calculated to evaluate the comprehensive performance of the DES ion kinetic promoter.[16] As shown in Fig. 1f and S3, the adsorption energy of PF_6^- anion on the LLZTO-F and LLZTO is −7.16 eV and −4.14 eV, respectively, indicating that the anions can be anchored on the DES ion kinetic promoter and the dissociation of Li salts can be accelerated. Meanwhile, with the introduction of the F atom, the adsorption energies of solvents, such as ethylene carbonate (EC) and diethyl carbonate (DEC), on the LLZTO-F are −0.22 eV and −0.72 eV, respectively, which are higher than those on the LLZTO (−0.18 eV and −0.22 eV).[17] Besides, the LLZTO-F has a lower desolvation energy barrier (1.95 eV) than that of LLZTO (2.13 eV), which enables the rapid desolvation of $Li(solvent)_x^+$ and avoids the local accumulation of Li^+ (Fig. 1g).[7,17,18] With lattice distortion and the increased number of active sites induced by F-substitution, Li rapidly migrates on the surface of LLZTO-F (0.80 eV), thereby avoiding Li dendrite growth (Fig. 1h). Thus, the calculations strongly suggest that introducing the DES ion kinetic promoter increases the interfacial/internal Li^+/Li^0 diffusion rates and balances the interfacial electrochemistry, thereby achieving satisfied electrochemical performance of LMBs.[19,20]

In our treatment (Fig. 2a), pristine LLZTO was exposed to HF vapor by heating NH_4F to transform into $LLZTO_xF_y$ DES ion kinetic promoter.[21] By regulating the NH_4F : LLZTO ratio, the atomic O/F ratio in $LLZTO_xF_y$ is adjusted, inducing local charge redistribution and forming a DES ion kinetic promoter with higher activity. After fluorination, an F signal was detected and gradually increased in X-ray photoelectron spectroscopy (XPS; Fig. S5), while the O signal decreased, indicating the successful formation of $LLZTO_xF_y$. For simplicity, these optimized samples with gradual conversion are identified as $LLZTO_{1.00}$, $LLZTO_{0.95}F_{0.05}$, $LLZTO_{0.91}F_{0.09}$, and $LLZTO_{0.71}F_{0.29}$, based on XPS. As shown in Fig. 2b, atomic F preferentially replaces the O site adjacent to La to form the La–F. Then, with the increase in F content, the characteristic peaks of Zr–F and Li–F gradually enhance while the Li–O decreases (Fig. S6a). Accordingly, we observe the characteristic peaks of Li 1s, Zr 3d, and Ta 4f shift towards the direction of high binding energy, indicating that the bonding strength is enhanced due to the formed M–F bond in $LLZTO_{0.71}F_{0.29}$, achieving strong separation of local charges-holes and improving interfacial charge transfer rate (Fig. S6a–d).[22] While the characteristic peak of La 3d shifts towards lower binding energies, indicating that the La site gains electrons and forms the unsaturated site metal. This result was also verified by O 1s (Fig. 2c). The components of $LLZTO_xF_y$ were further investigated by X-ray diffraction (XRD). The atomic F-substitution in $LLZTO_{0.95}F_{0.05}$ did not induce lattice distortion, effectively ensuring the stability of the DES ion kinetic promoter (Fig. 2d). With the O/F ratio reaching approximately 9 : 1, the characteristic peak of LaF_3 (45.0°) emerges in $LLZTO_{0.91}F_{0.09}$. Therefore, it can be inferred that F preferentially substitutes the O site adjacent to La, thereby constructing a metastable F–La–O_3 structure. With the further substitution of the F atom, distinct peaks of Li_4ZrF_8 and LaF_3 emerge in $LLZTO_{0.71}F_{0.29}$. Although both slightly soluble LaF_3 and Li_4ZrF_8 help stabilize the Li anode, their formation is generally regarded as detrimental to interfacial stability, as it leads to the collapse of the $LLZTO_xF_y$ structure and an increase in defects.[23,24]

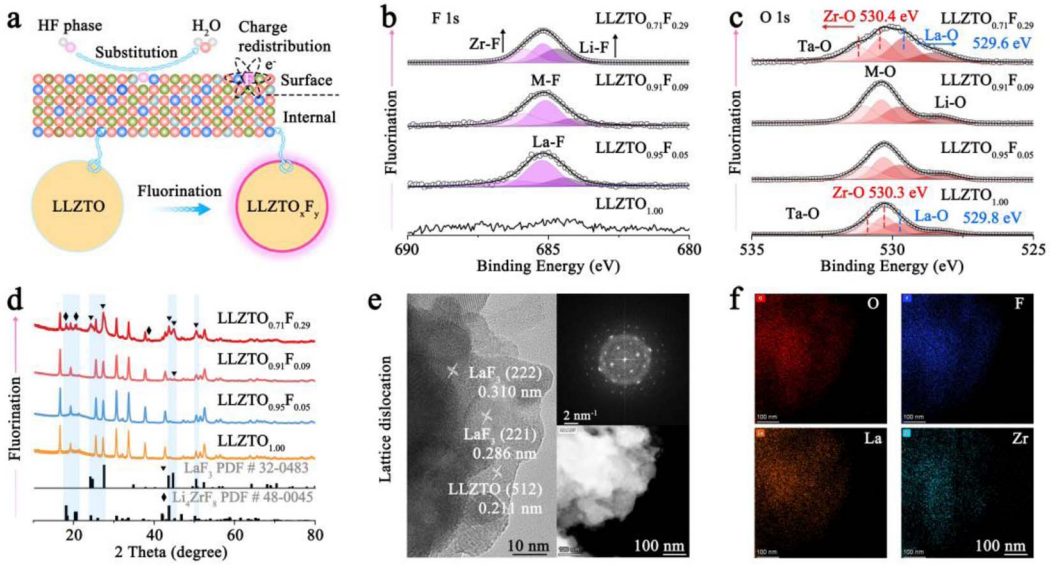

Fig. 2 (a) Schematic illustration of vapor-phase fluoride treatment. The comparisons of (b) F 1s, (c) O 1s XPS spectra, and (d) XRD of $LLZTO_xF_y$. (e) HRTEM images and (f) elemental mappings of the $LLZTO_{0.95}F_{0.05}$.

The microstructure of the $LLZTO_xF_y$ DES ion kinetic promoter was analyzed using scanning electron microscopy (SEM) and high-resolution transmission electron microscopy (HRTEM). As shown in Fig. S7, with the substitution of F atoms, $LLZTO_{1.00}$ gradually transforms from square particles to spherical particles ($LLZTO_{0.71}F_{0.29}$) with low surface energy, which was also preliminarily verified by elemental analysis (Fig. S8–11).[25] The HRTEM further characterized the phase evolution of $LLZTO_xF_y$. The lattice fringes and diffraction rings of $LLZTO_{0.95}F_{0.05}$ are more distinct than those in $LLZTO_{1.00}$ due to the repair of intrinsic defects by F-substitution. Meanwhile, the lattice interlacing on the surface of $LLZTO_{0.95}F_{0.05}$ indicates the presence of multiple phases corresponding to the XRD. As shown in Fig. 2e, the lattice spacings are 0.310, 0.286, and 0.211 nm, which are consistent with the (221), (222) planes of LaF_3 and the (512) plane of $LLZTO_{1.00}$, respectively. As the substitution of F increases gradually, the substantial formation of slightly soluble LaF_3 leads to structural degradation in both $LLZTO_{0.91}F_{0.09}$ and $LLZTO_{0.71}F_{0.29}$, which will cause the deactivation of the ion kinetic promoter during the electrochemical process (Fig. 2f and S12–14). Therefore, atomic-level F-substitution is beneficial for improving structural stability and achieving persistent regulation of interfacial ion transport.

A separator with micro-level pores is crucial for transmitting ions in liquid-state LMBs (Fig. S15). However, the $Li(solvent)_x^+$ can also pass through the micron pores of the separator freely.[18] Therefore, the $LLZTO_xF_y$ was coated on the commercial PP separator (Fig. S16) to promote rapid desolvation and accelerate interfacial ion transport. Moreover, the $LLZTO_xF_y$ modification layer improves electrolyte wettability relative to the PP separator (10.9° *vs.* 26.6°), thereby reducing interfacial resistance (Fig. S17). Besides, the introduction of atomic F induces local charge redistribution, anchoring anions and solvents, thereby releasing more free Li^+ (Fig. S18), consistent with theoretical calculations. Moreover, the introduction of the $LLZTO_xF_y$ modification layer contributes to the construction of a composite separator with improved physical/chemical stability (Fig. S19).[26]

Symmetric cells were assembled to evaluate the regulation of interfacial ion desolvation and transport nucleation during the electrochemical process.[27] Fig. 3a and S20 show that the Li||Li symmetric cell with $LLZTO_{0.95}F_{0.05}$@PP exhibits a higher Li^+

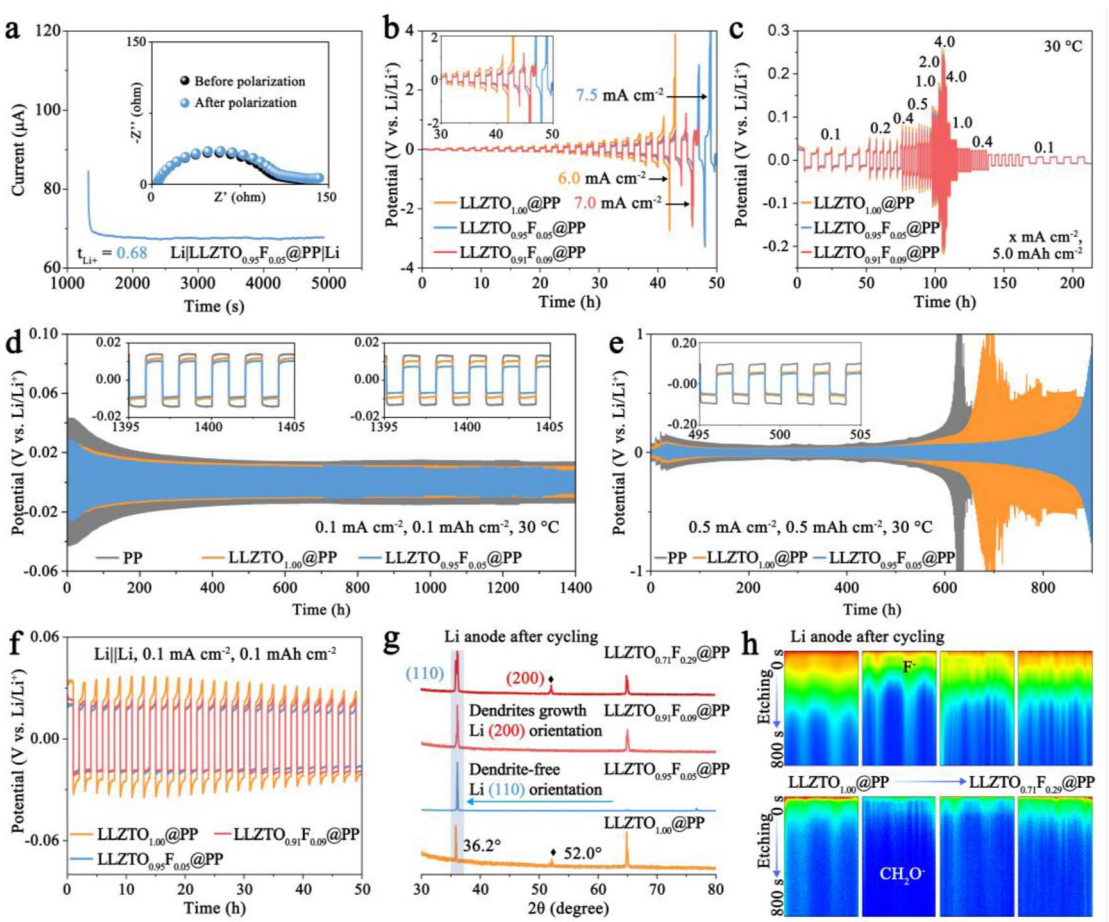

Fig. 3 (a) Current–time curves of the Li|$LLZTO_{0.95}F_{0.05}$@PP|Li symmetric cell with a perturbation of 10 mV. (b) Critical current density values and (c) rate performance of Li||Li symmetric cells at 0.1–4.0 mA cm^{-2}, 5.0 mAh cm^{-2}. Galvanostatic voltage profiles of Li||Li symmetric cells using different $LLZTO_xF_y$@PP at (d and f) 0.1 mA cm^{-2}, 0.1 mAh cm^{-2} and (e) 1.0 mA cm^{-2}, 1.0 mAh cm^{-2}, at 30 °C.(g) XRD and (h) TOF-SIMS of the Li metal within Li|$LLZTO_xF_y$@PP|Li symmetric cells after cycling.

transference number (t_{Li^+} = 0.68) than that of $LLZTO_{1.00}$@PP (0.58) and PP (0.32) due to the high anion adsorption energy. With the low desolvation energy barrier and interfacial ion migration energy barrier, the $LLZTO_{0.95}F_{0.05}$@PP-based Li||Li symmetrical cell exhibits a critical current density of 7.5 mA cm^{-2}, much higher than that with $LLZTO_{1.00}$ (6.0 mA cm^{-2}) and PP (5.0 mA cm^{-2}, Fig. 3b and S21). On the contrary, excessive F-substitution induces lattice distortion and structural collapse in $LLZTO_{0.95}F_{0.05}$ due to LaF_3 dissolution, leading to continuous interface deterioration and local dendritic Li growth, ultimately resulting in a short circuit (Fig. S22).[28] The rate performance shown in Fig. 3c indicates that introducing atomic F reduces the nucleation overpotential by lowering the interfacial Li nucleation energy barrier. Among them, the initial electroplating polarization voltages of $LLZTO_{0.95}F_{0.05}$@PP-based Li||Li symmetrical cell at 0.1, 0.2, 0.4, 0.5, 1.0, 2.0, and 4.0 mA cm^{-2} are 23.0, 24.6, 37.0, 40.7, 71.4, 119.3, and 201.7 mV, respectively. When the current density recovered to 0.1 mA cm^{-2}, a low polarization potential of 6.8 mV was still retained at 213 h without short circuit (Fig. S23). Moreover, at a current density of 0.1 mA cm^{-2}, 0.5 mA cm^{-2}, and the capacities of 0.1 mAh cm^{-2}, 0.5 mAh cm^{-2} were selected to investigate the long cycle stability of the $LLZTO_xF_y$ DES ion kinetic promoter. The $LLZTO_{0.95}F_{0.05}$@PP can stably plate/strip for 1400 h with low over-potential (7.3 mV) at 0.1 mA cm^{-2} (Fig. 3d and S24). Even under the current density of 0.5 mA cm^{-2}, the $LLZTO_{0.95}F_{0.05}$-based symmetrical cell achieves uniform interfacial Li atom nucleation for over 900 h (Fig. 3e and S25). By contrast, continuous interface deterioration and local Li nucleation result in short circuits in $LLZTO_{1.00}$@PP (650 h) and $LLZTO_{0.91}F_{0.09}$@PP (880 h).

To further reveal the role of $LLZTO_xF_y$ DES ion kinetic promoter in interfacial regulation, it is crucial to clarify the evolution of the Li nucleation morphology during electrodeposition. The Li|$LLZTO_xF_y$@PP|Li symmetric cells were tested under 25 cycles, and the composition changes of the cycled-Li anodes were investigated (Fig. 3f and S26). As shown in Fig. 3f, g and S27a, b, the delocalized electron-shared layer decreases the interfacial ion-migration energy barrier, accelerating rapid interfacial Li^+/Li^0 migration and enabling uniform Li^0 nucleation.[29,30] By contrast, $LLZTO_{1.00}$—with a large desolvation energy barrier and Li^0 migration energy barrier—induces Li^0 nucleation on the (200) crystal plane and vertical Li dendrites growth, which is manifested as nanoparticles in the SEM image (Fig. S27b1).[31] Meanwhile, during plating/stripping, the structural collapse of $LLZTO_{0.71}F_{0.29}$ leads to continuous interface deterioration and dendrite growth, ultimately resulting in a continuous increase in polarization potential and

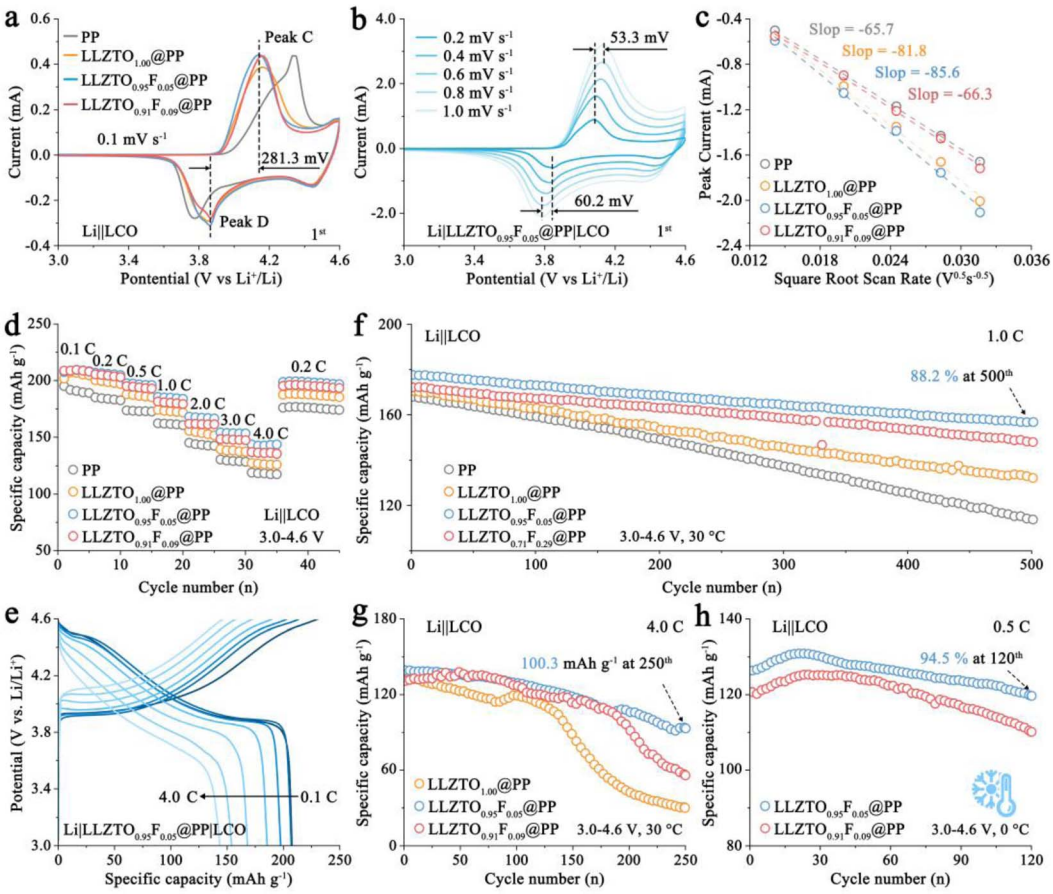

Fig. 4 (a and b) CV curves of Li|$LLZTO_xF_y$@PP|LCO. (c) Plots of logarithm peak current *versus* logarithm scan rates. (d and e) Rate capability and cycling performance of Li||LCO cells with different $LLZTO_xF_y$@PP at (f) 1.0C, (g) 4.0C, and (h) 0.5C.

substantial Li dendrite growth (Fig. 3g and S27b4). The structural evolution of the solid electrolyte interphase (SEI) layer at the Li anode-electrolyte interface during electrochemical processes is critical for regulating interfacial ion transport and Li deposition behavior. The component distribution of SEI was further confirmed by time-of-flight secondary ion mass spectrometry (TOF-SIMS). For the SEI on the cycled Li metal protected by the $LLZTO_{1.00}$ and $LLZTO_{0.71}F_{0.29}$, the dense LiF layer with a high interfacial Li^+ diffusion energy barrier forms on the surface of SEI (Fig. 3h).[32] Conversely, the distribution of LiF and Li_2O in Fig. 3h and S28 indirectly demonstrates that interfacial degradation of the Li anode and electrolyte decomposition can be inhibited with the anchoring effect of $LLZTO_{0.95}F_{0.05}$.[33] Meanwhile, the content and distribution of the CH_2O^- further corroborate the aforementioned viewpoint.[34] Therefore, atomic F-substitution will induce charge redistribution in the central La atoms, thereby enhancing local charge transport in $LLZTO_{0.95}F_{0.05}$ and, consequently, achieving rapid interfacial ion transport and uniform Li^0 deposition.

The high-voltage full cells were assembled to investigate the electrochemical performance of the DES ion kinetic promoter.[35,36] The cyclic voltammogram (CV) in Fig. 4a shows that the Li|$LLZTO_{0.95}F_{0.05}$@PP|LCO exhibits high redox peak current and low redox voltage (281.3 mV) at 0.1 mV s^{-1}. Meanwhile, the polarization voltage of the oxidation and reduction peaks of the Li|$LLZTO_{0.95}F_{0.05}$@PP|LCO cell is only 53.3 mV and 60.2 mV, respectively, which are much lower than those of the cells with $LLZTO_{1.00}$ (83.3 mV, 70.0 mV) and PP (113.6 mV, 83.0 mV), from 0.2 mV s^{-1} to 1.0 mV s^{-1} (Fig. 4b and S29). This further indicates the $LLZTO_{0.95}F_{0.05}$ DES ion kinetic promoter contributes to enhance the interfacial Li^+ transport and enables rapid Li^0 migration on the surfaces of the anode and cathode (Fig. 4c). The initial specific capacities of the Li|$LLZTO_{0.95}F_{0.05}$@PP|LCO cell at 0.1, 0.2, 0.5, 1.0, 2.0, 3.0, and 4.0C are 207.6, 207.0, 197.6, 185.6, 168.1, 154.2, and 143.6 mAh g^{-1}, respectively (Fig. 4d, e and S30). When the current density is restored to 0.2C, it still maintains a high specific capacity of 198.8 mAh g^{-1}, which is much higher than those of the Li||LCO

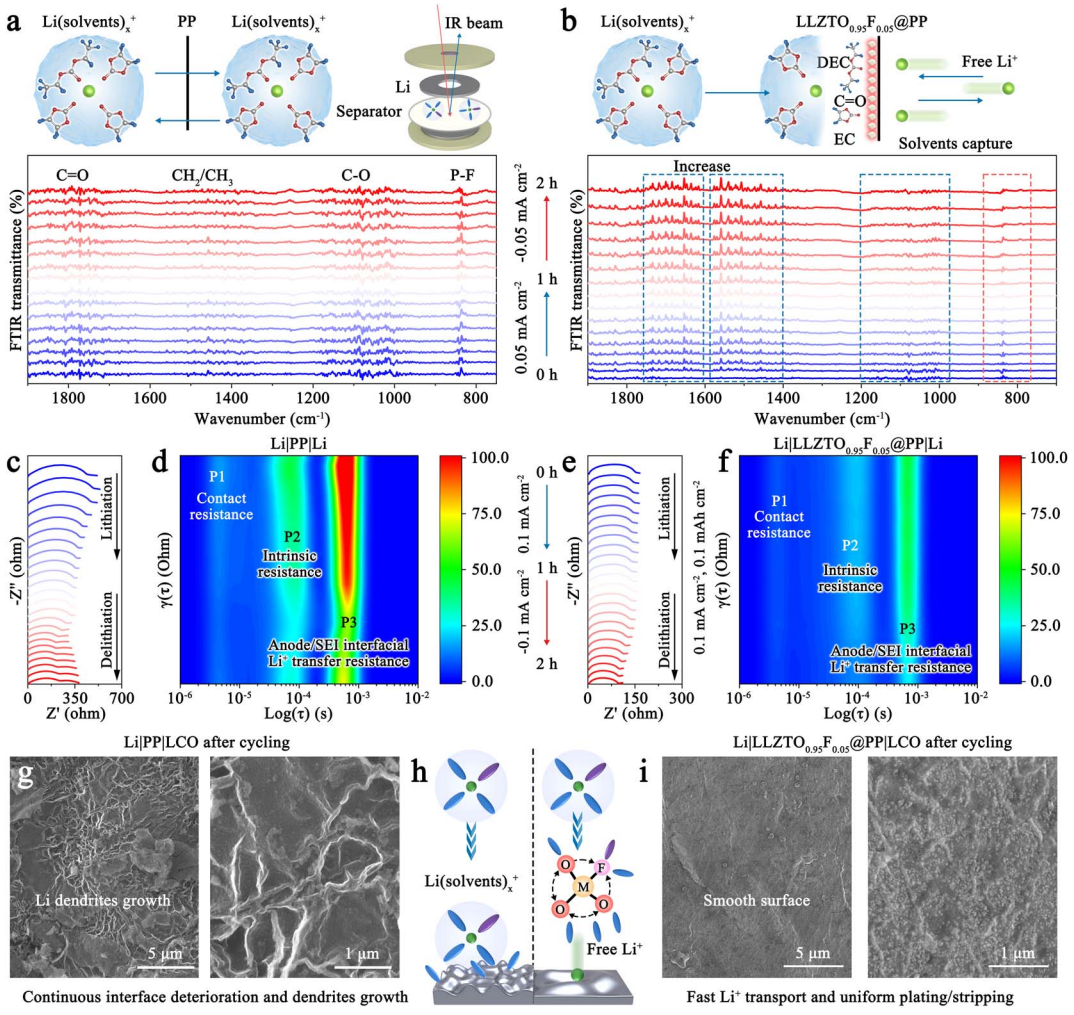

Fig. 5 (a and b) *In situ* FTIR spectroscopy reveals the solvation structure evolution of Li(solvent)$_x^+$ in Li||Li symmetric cells. *In situ* (c) EIS and (d) DRT of Li|PP|Li. *In situ* (e) EIS and (f) DRT of Li|$LLZTO_{0.95}F_{0.05}$@PP|Li. (g and i) SEM images of cycled Li anode in Li||LCO at 20th under 0.2C. (h) Schematic diagram of the desolvation mechanism of DES ion kinetic promoter.

with PP (176.1 mAh g^{-1}) and LLZTO@PP (187.5 mAh g^{-1}) at the 36th cycle. Meanwhile, with the improved interfacial ion transport rate and interface stability, the Li|$LLZTO_{0.95}F_{0.05}$@-PP|LCO cell retains a high specific capacity of 88.2% after 500 cycles at 1.0C. Still, it exhibits a high specific capacity of 100 mAh g^{-1} after 250 cycles at 4.0C (Fig. 4f and g). Moreover, the Li|$LLZTO_{0.95}F_{0.05}$@PP|LCO cell maintains a capacity retention rate of 94.5% after 120 cycles at 0.5C, further confirming that the DES ion kinetic promoter can desolvate and accelerate interfacial ion transport even at low temperatures (Fig. 4h).[37] Therefore, the $LLZTO_{0.95}F_{0.05}$ DES ion kinetic promoter accelerates desolvation kinetics, enabling a long-lasting, stable Li metal anode.

To understand the key role of the DES ion kinetic promoter in enhancing LMB performance, *in situ* FTIR was used to investigate the solvation structure evolution of $Li(solvent)_x^+$ on $LLZTO_{0.95}F_{0.05}$. Fig. 5a reveals that the solvation structure of $Li(solvent)_x^+$ remained unchanged. By contrast, distinct C=O (1750–1600 cm^{-1}) and CH_2/CH_3 (1600–1400 cm^{-1}) infrared characteristic peaks can be detected on the $LLZTO_{0.95}F_{0.05}$@PP separator (Fig. 5b).[38,39] Furthermore, under the applied electric field, the peak of C=O and CH_2/CH_3 is increased, which indicates that solvent molecules (EC and DEC) have been captured by $LLZTO_{0.95}F_{0.05}$, thereby releasing additional free Li^+ and accelerating interfacial Li^+ transport kinetics. While, due to the inherently limited desolvation kinetics of $LLZTO_{1.00}$, solvents will still shuttle freely under the electric field (Fig. S31). Subsequently, *in situ* electrochemical impedance spectroscopy (EIS) and distribution of relaxation times (DRT) fitting were performed.[40] The poor interfacial contact between the PP separator and the electrolyte results in a high interfacial charge-transfer resistance, leading to elevated contact resistance (10^{-6} to 10^{-5} s) and an inherent internal resistance (10^{-5} to 10^{-4} s; Fig. 5c, d and S32a, b). Concurrently, sluggish ion transport and a high interfacial desolvation energy barrier for $Li(solvent)_x^+$ result in significant interfacial transmission impedance (10^{-4} to 10^{-3} s) in the Li|PP|Li symmetric cell. Conversely, $LLZTO_{0.95}F_{0.05}$ facilitates rapid desolvation of interfacial $Li(solvent)_x^+$, promoting efficient Li^+ diffusion and transport (Fig. 5e, f and S32c, d).

To further elucidate the working mechanism of $LLZTO_{0.95}F_{0.05}$ DES ion kinetic promoter, cycled Li anodes were disassembled and characterized. Fig. 5g and h demonstrates that the coexistence of free solvent molecules and sluggish interfacial Li^+ transport degrades the Li metal, promoting the formation of sheet-like Li dendrites.[27] By contrast, with the introduction of $LLZTO_{0.95}F_{0.05}$ DES ion kinetic promoter, the Li deposition occurred *via* fine-grained growth, contributing to the long-cycling stability (Fig. 5i). Consequently, this DES ion kinetic promoter-mediated desolvation strategy effectively promotes the long-cycle stability of LMBs.

Conclusion

In this work, a new concept, the delocalized-electron sharing ion kinetic promoter, is proposed to accelerate the desolvation of $Li(solvent)_x^+$. As a proof-of-concept model, various $LLZTO_xF_y$ DES ion kinetic promoters with different degrees of fluorination are systematically fabricated and investigated. Theoretical calculations reveal that F-substitution disrupts the equilibrium state of the M-O_4 structure, inducing charge redistribution on M-O_3-F and facilitating delocalized electron sharing. *In situ* FTIR and electrochemical experiments corroborate that the $LLZTO_{0.95}F_{0.05}$ DES ion kinetic promoter effectively anchors solvent molecules and anions, especially under the applied electric field, releasing free Li^+ and accelerating interfacial Li diffusion/nucleation kinetics. Consequently, the Li|$LLZTO_{0.95}$-$F_{0.05}$@PP|Li symmetrical cell can cycle for over 900 h under 0.5 mA cm^{-2} without short circuit. The Li||LCO with $LLZTO_{0.95}$-$F_{0.05}$@PP can still maintain a capacity retention rate of 94.5% at 120th at 0.5C under 0 °C. Our work has identified a new way to regulate the local electronic density, generating more active sites to accelerate interfacial kinetics and enabling practical LMBs.

Experimental section

Detailed experimental methods are provided in the supplementary information (SI).

Author contributions

Peng Chen conceived the idea, conducted the materials preparation, battery-related experiments, simulations, and prepared the draft manuscript. Bing Ding and Xiaogang Zhang participated in discussions. Hui Dou and Xiaogang Zhang contributed to manuscript editing, funding acquisition, and conceptualization.

Conflicts of interest

There are no conflicts to declare.

Data availability

All the data supporting this article have been included in the main text and the supplementary information (SI). Supplementary information is available. See DOI: https://doi.org/10.1039/d6sc02973f.

Acknowledgements

This work was supported by the National Natural Science Foundation Funded Project (52372199), National Key Research and Development Program of China (2023YFB2405800), Shenzhen Longhua Science and Technology Innovation Special Funding Project (Industrial Sci-Tech Innovation Center of Low-Altitude Intelligent Networking), Shenzhen Science and Technology Program (JCYJ20250604190043054), and Leading Edge Technology of Jiangsu Province (BK20232022, BK20220009). The authors thank the Center for Microscopy and Analysis at Nanjing University of Aeronautics and Astronautics for supporting the tests.

References

1 Q. Kang, Z. Zhuang, Y. Li, Y. Zuo, J. Wang, Y. Liu, C. Shi, J. Chen, H. Li, P. Jiang and X. Huang, *Nano Res.*, 2023, **16**, 9240–9249.
2 Y. Zang, P. Peng, F. Pei, R. H. Li, L. Wu, D. Q. Lu, Y. Zhang, K. Huang, Y. Shen, Y. H. Huang and Y. Q. Lan, *Natl. Sci. Rev.*, 2025, **12**, nwae443.
3 T. Wang, Y. Li, J. Zhang, K. Yan, P. Jaumaux, J. Yang, C. Wang, D. Shanmukaraj, B. Sun, M. Armand, Y. Cui and G. Wang, *Nat. Commun.*, 2020, **11**, 5429.
4 J. Dong, X. Cheng, H. Yang, H. Li, H. Liu, L. Jia, Y. Zhang, Q. Guan, J. Jia, F. Wu, J. Zhang, M. Liu, H. Lin and J. Wang, *Adv. Mater.*, 2025, **37**, 2501079.
5 Q. He, Z. Deng, S. Miao, Y. Jia, J. Peng, P. Xia, C. Xu, Q. Tang, X. Zhang, T. Tan, G. Zhu, K. Wu, Y. Fang, Y. Zhang and W. Cai, *Energy Environ. Sci.*, 2025, **18**, 9093–9104.
6 J. Xiao, *Science*, 2019, **366**, 426–427.
7 Y. Lin, J. Wang, X. Zhang, X. Cheng, Q. Zhuang, J. Zhang, Q. Guan, Y. Wang, C. Shen, H. Lin, L. Zhan, L. Ling and Y. Zhang, *Adv. Funct. Mater.*, 2025, **35**, 2501496.
8 S. Li, K. Huang, L. Wu, D. Xiao, J. Long, C. Wang, H. Dou, P. Chen and X. Zhang, *Chem. Sci.*, 2023, **14**, 10786–10794.
9 Z. Hu, Z. Han, H. Liu, X. Jiang, K. Bai, S. Huang, Z. Yang, M. Ye, Y. Tang, Y. Zhang, X. Liu, Z. Wen, H. S. Park and C. C. Li, *J. Am. Chem. Soc.*, 2025, **147**, 46632–46641.
10 R. Xu, A. Hu, W. Xu, W. Yang, F. Li, Y. Li, Y. Mu, L. Zeng, J. Long and S. Chen, *Angew Chem. Int. Ed. Engl.*, 2025, **64**, e202513321.
11 Y. He, D. Xiong, M. Chen, W. Zhang, S. Liu, Y. Ye, M. Wang, Y. Chen, Q. Tang, X. Peng, C. Wang, H. Zhan, H. Liu, M. Liu, J. Su, H. Shu, J. Wang and X. Wang, *Angew Chem. Int. Ed. Engl.*, 2025, **64**, e202512168.
12 P. Chen, T. Wang, D. He, T. Shi, M. Chen, K. Fang, H. Lin, J. Wang, C. Wang and H. Pang, *Angew Chem. Int. Ed. Engl.*, 2023, **62**, e202311693.
13 B. Wu, Z. Chen, Y. Ye, J. Z. Y. Seow, D. Mandler, A. Fisher, D. Wang, S. Guo and Z. J. Xu, *Chem. Soc. Rev.*, 2026, **55**, 114–143.
14 L. Chen, X. Guan, Z. Yao, S. Hayama, M. A. V. Spronsen, B. Karagoz, G. Held, D. G. Hopkinson, C. S. Allen, J. Callison, P. J. Dyson and F. R. Wang, *Nat. Commun.*, 2025, **16**, 9412.
15 J. Zhang, L. Pan, L. Jia, J. Dong, C. You, C. Han, N. Tian, X. Cheng, B. Tang, Q. Guan, Y. Zhang, B. Deng, L. Lei, M. Liu, H. Lin and J. Wang, *Nano Lett.*, 2025, **25**, 3756–3765.
16 J. Wang, J. Zhang, Y. Zhang, H. Li, P. Chen, C. You, M. Liu, H. Lin and S. Passerini, *Adv. Mater.*, 2024, **36**, 2402792.
17 B. Yang, Y. Wang, R. Zheng, W. Yang, Y. Li, T. Li, K. Li, A. Hu, J. Long and S. Ding, *Angew Chem. Int. Ed. Engl.*, 2025, **64**, e202508486.
18 J. Qin, F. Pei, R. Wang, L. Wu, Y. Han, P. Xiao, Y. Shen, L. Yuan, Y. Huang and D. Wang, *Adv. Mater.*, 2024, **36**, 2312773.
19 Q. Kang, Z. Zhuang, Y. Liu, Z. Liu, Y. Li, B. Sun, F. Pei, H. Zhu, H. Li, P. Li, Y. Lin, K. Shi, Y. Zhu, J. Chen, C. Shi, Y. Zhao, P. Jiang, Y. Xia, D. Wang and X. Huang, *Adv. Mater.*, 2023, **35**, 2303460.
20 P. Chen, P. Guo, W. Guo, B. Ding, H. Dou and X. Zhang, *J. Energy Chem.*, 2025, **110**, 363–371.
21 X. Zhao, P. Zang, T. Liu, Y. Jiang, J. Zhang, Y. Tang, B. Li, M. Xue, W. Zhang, Z. Zhang and W. Guo, *Science*, 2024, **385**, 433–438.
22 C. He, L. Yang, J. Wang, T. Wang, J. Ju, Y. Lu and W. Chen, *Carbon Energy*, 2024, **6**, e573.
23 W. Lin, Q. Gao, Y. Zhang, F. Zhang, Z. Huang, Q. Kang, Y. Liao, L. Wu, S. Hao, Y. Ren, F. Pei and Y. Huang, *J. Am. Chem. Soc.*, 2025, **147**, 43655–43665.
24 Q. Xu, T. Li, Z. Ju, G. Chen, D. Ye, G. I. N. Waterhouse, Y. Lu, X. Lai, G. Zhou, L. Guo, K. Yan, X. Tao, H. Li and Y. Qiu, *Nature*, 2025, **637**, 339–346.
25 X. Zhang, J. Li, T. Wang, Y. Gong and J. Zhou, *Nat. Commun.*, 2025, **16**, 5781.
26 S. Cai, X. Du, X. Gao, C. Zhao, C. Cheng, R. Lin, X. Yang, D. Luo, R. Sun and Z. Chen, *Nano Energy*, 2025, **140**, 111031.
27 Q. Yang, C. Wang, L. Song, Y. Zhang, Z. Shen, W. Cai and Y. Song, *Angew Chem. Int. Ed. Engl.*, 2025, **64**, e202415078.
28 K. Yan, Z. Lu, H.-W. Lee, F. Xiong, P.-C. Hsu, Y. Li, J. Zhao, S. Chu and Y. Cui, *Nat. Energy*, 2016, **1**, 16010.
29 G. Yang, Y. Li, C. Zhang, J. Wang, Y. Bai, C. Y. J. Lim, M. F. Ng, Z. Chang, S. Kumar, Z. Sofer, W. Liu and Z. W. Seh, *Nano Lett.*, 2022, **22**, 9138–9146.
30 Q. Yang, S. Shen, Z. Han, G. Li, D. Liu, Q. Zhang, L. Song, D. Wang, G. Zhou and Y. Song, *Adv. Mater.*, 2024, **36**, 2405790.
31 Z. Sun, Y. Wang, S. Shen, X. Li, X. Hu, M. Hu, Y. Su, S. Ding and C. Xiao, *Angew Chem. Int. Ed. Engl.*, 2023, **62**, e202309622.
32 S. Li, S. Fang, H. Dou and X. Zhang, *ACS Appl. Mater. Interfaces*, 2019, **11**, 20804–20811.
33 X. Chen, M. Jiang, X. Du, X. Gao, K. Feng, Y. Liu, X. Yang, R. Sun, D. Luo and Z. Chen, *Adv. Energy Mater.*, 2025, **15**, 2502589.
34 H. Ji, J. Xiang, Y. Li, M. Zheng, L. Yuan, Y. Liao, L. Du, Z. Li, Z. Xie, K. Huang, X. Lin, Z. Xie, Y. Shen, M. Chen, T. Li, G. Feng, Y. Sun, L. Qie, H. Li, F. Zhang, R. Guo, X. Feng, W. Chen, X. Ai, J. Lu and Y. Huang, *Nature*, 2025, **643**, 1255–1262.
35 Z. Hao, X. Liu, Y. Li, J. Liu, H. Li, L. Wang, G. Yang and J. Ma, *Adv. Energy Mater.*, 2025, **15**, 2502242.
36 X. Yang, Y. Lin, S. Tang, Y. Zhou, X. Huang, W. Song, W. Yang and Y. Yang, *Energy Storage Mater.*, 2025, **81**, 104473.
37 P. Chen, T. Huang, T. Wei, B. Ding, H. Dou and X. Zhang, *Adv. Funct. Mater.*, 2025, **35**, 2420351.
38 J. Wang, J. Zhang, X. Cheng, Y. Zhang, H. Li, Q. Guan, F. Wu, H. Li, D. Wang, M. Liu, Y. Zhang, Q. Xiao, S. Passerini and H. Lin, *J. Am. Chem. Soc.*, 2025, **147**, 44633–44651.
39 H. Luo, X. Ji, B. Zhang, M. Chen, X. Wu, Y. Zhu, X. Yu, J. Wang, H. Zhang, Y. Hong, Y. Zou, G. Feng, Y. Qiao, H. Zhou and S. G. Sun, *Angew Chem. Int. Ed. Engl.*, 2024, **63**, e202412214.
40 Y. Lu, C.-Z. Zhao, J.-Q. Huang and Q. Zhang, *Joule*, 2022, **6**, 1172–1198.